Interactions of Radiation, Microphysics, and Turbulence in the Evolution of Cirrus Clouds

YU GU AND K. N. LIOU

Department of Atmospheric Sciences, University of California, Los Angeles, Los Angeles, California

ABSTRACT

A two-dimensional cirrus cloud model has been developed to investigate the interaction and feedback of radiation, ice microphysics, and turbulence-scale turbulence, and their influence on the evolution of cirrus clouds. The model is designed for the study of cloud-scale processes with a 100-m grid spacing. The authors have incorporated a numerical scheme for the prediction of ice crystal size distributions based on calculations of nucleation, diffusional growth, advection, gravitational sedimentation, and turbulent mixing. The radiative effect on the diffusional growth of an individual ice crystal is also taken into account in the model. The model includes an advanced interactive radiative transfer scheme that employs the δ-four-stream approximation for radiative transfer, the correlated k-distribution method for nongray gaseous absorption, and the scattering and absorption properties of hexagonal ice crystals. This radiation scheme is driven by ice water content and mean effective ice crystal size that represents the ice crystal size distribution. To study the effects of entrainment and mixing on the cloud, a second-order turbulence closure has been developed and incorporated into the model. Simulation results show that initial cloud formation occurs through ice nucleation associated with dynamic and thermodynamic forcings. Radiation becomes important for cloud evolution once a sufficient amount of ice water is generated. Radiative processes enhance both the growth of ice crystals at the cloud top by radiative cooling and the sublimation of ice crystals in the lower region by radiative heating. The simulated ice crystal size distributions depend strongly on the radiation fields. In addition, the radiation effect on individual ice crystals through diffusional growth is shown to be significant. Turbulence begins to play a substantial role in cloud evolution during the maintenance and dissipation period of the cirrus cloud life cycle. The inclusion of turbulence tends to generate more intermediate-to-large ice crystals, especially in the middle and lower parts of the cloud. Incorporation of the second-order closure scheme enhances instability below the initial cloud layer and brings more moisture to the region above the cloud, relative to the use of the traditional eddy mixing theory.

1. Introduction

Cirrus clouds play an important role in the radiation field of the earth–atmosphere system and, hence, significantly affect the atmospheric thermal structure and climate (Liou 1986, 1992). This importance has been highlighted by a number of intensive composite field observations: the First International Satellite Cloud Climatology Project (ISCCP) Regional Experiment (FIRE) I in October–November 1986; FIRE II in November–December 1991; the European experiment on cirrus (ICE/EUCREX) in 1989; and Subsonic Aircraft: Contrail and Cloud Effect Special Study in April 1996. Fundamental understanding of the mechanisms for the formation, maintenance, and dissipation of cirrus in the atmosphere is still limited and requires in-depth studies from both observational and modeling perspectives.

Several attempts have been made to develop numerical models to investigate the role of various physical processes in the life cycle of cirrus clouds. For example, Jensen et al. (1994a,b) used a one-dimensional cirrus cloud formation model that includes explicit simulation of the size distribution of ice crystals involving a number of microphysical processes. Although their model produces reasonable ice water content (IWC), the prediction for ice crystal number densities appears to be too low. Because of their simple dynamics, one-dimensional models have been employed extensively by researchers whose interests focus on complex microphysical processes (e.g., Heymsfield and Sabin 1989; Chen et al. 1997).

Cirrus clouds are a dynamic and thermodynamic system that involves the intricate coupling of microphysics, radiation, and dynamic processes (Gultepe and Starr 1995). A multidimensional setting is thus required for interaction and feedback studies. In their pioneering work, Starr and Cox (1985) developed a two-dimensional (2D) model and showed that the effects of radiative processes and vertical transports are both significant in cirrus cloud formation and maintenance. Gu and Liou (1997a,b) constructed a 2D cirrus model that includes a second-order turbulence closure and found that turbulence can significantly modulate the supersaturation condition and hence affect the rate at which water vapor is converted to ice. However, ice micro-

Corresponding author address: Prof. K. N. Liou, Department of Atmospheric Sciences, University of California, Los Angeles, Los Angeles, CA 90095.
E-mail: knliou@atmos.ucla.edu

physical processes are parameterized in terms of IWC in these models in which the excess moisture is entirely converted to IWC in just one time step. More recently, Lin (1997) and Khvorostyanov and Sassen (1998a) have incorporated explicit microphysics schemes in 2D models for the simulation of ice crystal size distributions.

The exchange coefficient or the first-order closure approach has been commonly used in modeling turbulence associated with cirrus cloud processes. A number of studies reveal that turbulent mixing plays the dominant role in the evolution of the lower-tropospheric clouds (Telford and Wagner 1981; Baker and Latham 1979; Paluch and Knight 1984). The study of Moeng (1986) using a large eddy simulation model showed that turbulence plays a rather important role in the structure of the stratus-topped boundary layer. Also, numerical simulations of stratiform (altocumulus) clouds performed by Liu and Krueger (1998) showed that moist conservative variables in the altocumulus layer are approximately well mixed. In cirrus cloud conditions, radiative heating or cooling and latent heat release can act as sources of turbulence. Quante et al. (1990) demonstrated the presence of turbulence in cirrus based on the data obtained from the previously mentioned ICE/EUCREX experiment. Gultepe and Starr (1995) used the aircraft observations during FIRE to analyze the dynamic structure and turbulence in cirrus clouds. They concluded that the intermediate-scale waves observed in the atmosphere can play an important role in the development of the cirrus cloud system. The cellular structure found in Starr and Cox's cirrus cloud simulations also implies the occurrence of turbulence.

The preceding observations suggest that a higher-order closure for turbulence is needed to investigate the effect of turbulence on ice microphysics, which can feed back to radiative cooling. This feedback process could be significant in the maintenance of cirrus clouds and has not been studied at this point. Ideally, numerical simulations of cirrus cloud dynamics should be conducted using a three-dimensional (3D) model. However, because of the substantial increase in the number of prognostic variables when an explicit ice microphysics scheme is used, and because of the limitation of computer resources, 2D cloud models are usually adopted for cloud process studies. Moreover, Moeng et al. (1996) showed that 2D cloud-resolving models can produce excellent predictions for the virtual potential temperature, total water mixing ratio, and liquid water mixing ratio in comparison to those generated from 3D large eddy simulation models for stratocumulus.

To study the physical processes governing the evolution of cirrus clouds, we have developed a 2D model that includes a second-order turbulence closure scheme, the explicit prediction of ice crystal size distribution, and an advanced radiation parameterization. We have also included in the model the radiation effect on the formation of an individual ice crystal. Systematic description of the model is presented in section 2. Pertinent results from the model simulation are discussed in section 3.

2. Cirrus cloud model

a. Governing equations

For the modeling of stratiform cirrus clouds, it appears physically appropriate to consider two-dimensional space and utilize the Boussinesq approximation under which the fluid is treated as incompressible; that is, air density is considered to be a constant except when it is coupled with gravity in the buoyancy term of the vertical momentum equation. The requirement to satisfy this approximation is that the depth of convection must be much smaller than the scale height of the basic state, which is about 8 km. Note that the convective region of cirrus studied in this paper has a depth of around 1 km during the entire simulation period. We have also neglected the Coriolis term in view of the fact that the motion in cirrus is small-scale. Let us consider now a cloud-free initial state that is horizontally uniform and at rest except for a constant vertical motion w_0. Since turbulence plays an important role in the formation and dissipation of stratus and stratiform clouds (Moeng 1980; Liu and Krueger 1998), a second-order turbulence closure is further incorporated in the formulation of the model. We shall also include explicitly the evolution of ice crystal size distribution in the cirrus cloud model. Based on the preceding considerations, the mean field equations for dynamic and thermodynamic variables in the x–z plane can be expressed in the following forms:

$$\frac{\partial u}{\partial t} = -u\frac{\partial u}{\partial x} - (w_0 + w)\frac{\partial u}{\partial z} - \frac{1}{\rho}\frac{\partial p}{\partial x} - \frac{\partial}{\partial x}\overline{u'^2}$$
$$- \frac{\partial}{\partial z}\overline{u'w'}, \quad (2.1)$$

$$\frac{\partial w}{\partial t} = -u\frac{\partial w}{\partial x} - (w_0 + w)\frac{\partial w}{\partial z} - \frac{1}{\rho}\frac{\partial p}{\partial z} + gB$$
$$- \frac{\partial}{\partial x}\overline{u'w'} - \frac{\partial}{\partial z}\overline{w'^2}, \quad (2.2)$$

$$\frac{\partial u}{\partial x} + \frac{\partial w}{\partial z} = 0, \quad (2.3)$$

$$\frac{\partial \theta}{\partial t} = -u\frac{\partial \theta}{\partial x} - (w_0 + w)\frac{\partial(\theta_0 + \theta)}{\partial z}$$
$$+ \pi^{-1}(Q_C + Q_R) - \frac{\partial}{\partial x}\overline{u'\theta'} - \frac{\partial}{\partial z}\overline{w'\theta'}, \quad (2.4)$$

$$\frac{\partial q}{\partial t} = -u\frac{\partial q}{\partial x} - (w_0 + w)\frac{\partial(q_0 + q)}{\partial z} - C$$
$$- \frac{\partial}{\partial x}\overline{u'q'} - \frac{\partial}{\partial z}\overline{w'q'}, \quad (2.5)$$

$$\frac{\partial n_i}{\partial t} = -\frac{\partial}{\partial m}\left[n_i\frac{dm_i}{dt}\right] - \frac{\partial}{\partial x}[un_i]$$
$$- \frac{\partial}{\partial z}[(w + w_0 - U_f)n_i] + \left[\frac{\partial n_i}{\partial t}\right]_{nuc}$$
$$- \frac{\partial}{\partial x}\overline{u'n_i'} - \frac{\partial}{\partial z}\overline{w'n_i'}, \quad (2.6)$$

where n_i is the number density of ice crystals for the ith size group, m_i is the mean mass of the individual particle in the ith size group, the first term on the right-hand side of Eq. (2.6) represents the diffusional growth, and the fourth term is the initial nucleation contribution. The unsubscripted variables represent the resolved components with respect to a prescribed background (initial) state, which is denoted by subscript 0. Variables with primes stand for unresolved turbulent fluctuations, and $\pi = (p_0/p_r)^{R/c_p}$, with $p_r = 1000$ mb. The buoyancy term B in Eq. (2.2) can be represented by the potential temperature θ, including the specific humidity of water vapor q and ice water mixing ratio q_c in the form

$$B = \frac{\theta}{\theta_0} + \varepsilon'q - q_c, \qquad (2.7)$$

where $\varepsilon' = (1 - \varepsilon)/\varepsilon$, and ε is the ratio of the molecular weight of water to that of dry air. A number of terms appearing in the above equations will be defined in the following.

It is convenient to employ the vorticity equation in the formulation of stratus cloud models. This can be done by subtracting the derivative of Eq. (2.1) with respect to z from the derivative of Eq. (2.2) with respect to x and using the continuity equation. The use of vorticity eliminates the pressure gradient force terms denoted in Eqs. (2.1) and (2.2). Furthermore, we can express $u = -\partial\psi/\partial z$ and $w = \partial\psi/\partial x$, where ψ is the streamfunction. In terms of vorticity ζ, streamfunction ψ, and Jacobian J, the governing equations for the cirrus cloud formation model can be expressed by

$$\frac{\partial\zeta}{\partial t} = J(\zeta, \psi) - w_0\frac{\partial\zeta}{\partial z} + g\frac{\partial B}{\partial x} + \frac{\partial^2(\overline{u'w'})}{\partial z^2}$$
$$- \frac{\partial^2(\overline{u'w'})}{\partial x^2} + \frac{\partial^2(\overline{u'^2})}{\partial x\partial z} - \frac{\partial^2(\overline{w'^2})}{\partial x\partial z}, \qquad (2.8)$$

$$\frac{\partial\theta}{\partial t} = J(\theta + \theta_0, \psi) - w_0\frac{\partial(\theta + \theta_0)}{\partial z}$$
$$+ \pi^{-1}(Q_C + Q_R) - \frac{\partial(\overline{w'\theta'})}{\partial z} - \frac{\partial(\overline{u'\theta'})}{\partial x}, \qquad (2.9)$$

$$\frac{\partial q}{\partial t} = J(q + q_0, \psi) - w_0\frac{\partial(q + q_0)}{\partial z} - C$$
$$- \frac{\partial(\overline{w'q'})}{\partial z} - \frac{\partial(\overline{u'q'})}{\partial x}, \qquad (2.10)$$

$$\frac{\partial n_i}{\partial t} = -\frac{\partial}{\partial m}\left[n_i\frac{dm_i}{dt}\right] - \frac{\partial}{\partial x}[un_i]$$
$$- \frac{\partial}{\partial z}[(w + w_0 - U_f)n_i] + \left[\frac{\partial n_i}{\partial t}\right]_{\text{nuc}}$$
$$+ k_m\nabla^2 n_i, \qquad (2.11)$$

where

$$\zeta = \nabla^2\psi = \frac{\partial w}{\partial x} - \frac{\partial u}{\partial z},$$

$$J(F, \psi) = \frac{\partial F}{\partial x}\frac{\partial\psi}{\partial z} - \frac{\partial F}{\partial z}\frac{\partial\psi}{\partial x}, \quad \text{with } F = \zeta, \text{ or } \theta, \text{ or } q.$$

Due to the uncertainty of dealing with the turbulence effect on an individual ice crystal based on the second-order turbulence closure, we have used the eddy diffusion approximation in Eq. (2.11) in the present model, with k_m the eddy diffusivity for ice crystals set as 3 m^2 s^{-1} (Deardorff 1972; Klemp and Wilhelmson 1978; Lin 1997). The vorticity, potential temperature, and specific humidity are connected to the ice crystal size spectrum via the ice water mixing ratio q_c, the heating rate due to phase change Q_C, and the deposition–sublimation between water vapor and ice water C in the forms

$$q_c = \sum_{i=1}^{N} n_i m_i, \qquad (2.12)$$

$$Q_C = \frac{L_s C}{C_p}, \qquad (2.13)$$

$$C = C_{\text{dif}} + C_{\text{nuc}} = \sum_{i=1}^{N} n_i\frac{dm_i}{dt} + m_1\left[\frac{\partial n_1}{\partial t}\right]_{\text{nuc}}, \qquad (2.14)$$

where we have discretized the ice crystal size spectrum by N bins. In Eqs. (2.12)–(2.14), C_p is the specific heat at constant pressure; L_s is the latent heat of sublimation; and C_{dif} and C_{nuc} represent sources and sinks of moisture due to diffusional growth and nucleation of ice crystals, respectively. The ice crystals initially generated by nucleation are denoted by the mass of the smallest size group m_1. It follows that C_{nuc} is the product of m_1 and the rate of change of number density of ice crystals due to nucleation in this size group, and $C_{\text{nuc}} = 0$ when the nucleation process is terminated.

Finally, the governing equations (2.8)–(2.11) require seven turbulent fluxes denoted by the overbars, which can be predicted using the second-order closure based on prognostic equations for the second moments. The closure details are given in appendix A.

b. Radiative transfer parameterizations

Radiative heating, Q_R, is computed from a radiative transfer scheme that is based on the delta-four-stream approximation developed by Liou et al. (1988) for inhomogeneous cloudy atmospheres. The incorporation of nongray gaseous absorption is based on the correlated k-distribution method developed by Fu and Liou (1992). In this method, the cumulative probability of the absorption coefficient in a spectral interval is used to replace wavenumber as an independent variable. Monochromatic solutions of the radiative transfer equation for a multiple-scattering atmosphere can be used in connection with a given cumulative probability. The min-

imum number of quadrature points in the cumulative probability space ranges from 1 to about 10 for different absorbing gases in different spectral regions.

In the parameterization, the solar and IR spectra are divided into a number of spectral intervals according to the location of absorption bands. These are 0.2–0.69, 0.69–1.3, 1.3–1.9, 1.9–2.5, 2.5–3.5, and 3.5–5.0 μm for the solar spectrum, and 2200–1900, 1900–1700, 1700–1400, 1400–1250, 1250–1100, 1100–980, 980–800, 800–670, 670–540, 540–400, 400–280, and 280–10 cm^{-1} for the IR spectrum. Absorption due to H_2O (2500–14 500 cm^{-1}), O_3 (ultraviolet and visible), CO_2 (2850–5250 cm^{-1}), and O_2 (A, B, and γ bands) is accounted for in the solar spectrum. In the thermal infrared spectrum, absorption due to H_2O (0–2200 cm^{-1}), O_3 (980–1100 cm^{-1}), CO_2 (540–800 cm^{-1}), CH_4 (1100–1400 cm^{-1}), and N_2O (1100–1400 cm^{-1}) is included. The continuum absorption of H_2O is incorporated in the spectral region 280–1250 cm^{-1}. Using the correlated k-distribution method, 121 spectral calculations are required for each vertical profile in the present study.

The single-scattering properties of hexagonal ice crystals are computed from the parameterization using a mean effective size (D_e) to represent the ice crystal size distribution in radiative transfer calculations given by Fu and Liou (1993):

$$D_e = \int D \cdot DL \cdot n(L) \, dL \Big/ \int DL \cdot n(L) \, dL, \quad (2.15)$$

where D and L are the width and length of an ice crystal, respectively; and $n(L)$ represents the ice crystal size distribution. The width D can be related to length L according to aircraft observations (Auer and Veal 1970). The empirical relationships were derived by using over 1500 natural ice crystals with different shapes and sizes ranging from 15 μm to 1 cm. Because data are not available for ice crystals less than 15 μm, we have used the same parameterization for these sizes. Based on physical principles, the extinction coefficient normalized by IWC, the single-scattering albedo, and the expansion coefficients in the phase function may be expressed by third-degree polynomials in terms of $1/D_e$. The coefficients in the polynomials that are wavelength dependent are determined by numerical fitting to the exact results obtained from the light-scattering and absorption programs using 11 observed ice crystal size distributions (Takano and Liou 1989; Fu and Liou 1993). The single-scattering parameterization is performed for the 6 solar and 12 IR bands mentioned above. The radiation parameterization program is driven by the mean effective ice crystal size and the ice water path, which is the product of cloud thickness and IWC determined from

$$\text{IWC} = \rho \sum_i n(m_i) m_i, \quad (2.16)$$

where $n(m_i)$ is computed from the model and ρ is the air density.

c. The ice microphysics scheme

To investigate the intricate interaction and feedback between radiative processes and ice microphysics, we require a detailed microphysical model for the simulation of ice crystal size distribution from which the mean effective size can be computed. Included in this model are the heterogeneous deposition nucleation, diffusional growth, advection, gravitational sedimentation, and eddy diffusion of individual ice particles. Several physical factors are involved in the governing equations: radiation, saturation ratio, air temperature, and horizontal and vertical motion. The first term on the right-hand side of Eq. (2.11) represents the net accumulation of ice crystal number density of a particular size due to diffusional growth. The second term is the contribution from horizontal advection, while the third term is the vertical convergence of ice crystal number density determined by vertical air motion and ice crystal terminal velocity U_f. The fourth and fifth terms denote the nucleation source and eddy diffusion contributions, respectively. To seek solutions for the evolution of ice crystal size distributions, the ice crystal length spectrum is discretized into a finite number of intervals (bins) of 15 μm. A partial differential equation can then be expressed for each bin and solved numerically. The mean mass of ice crystals of each size group can be calculated based on the parameterization relationships developed by Ramaswamy and Detwiler (1986).

1) DIFFUSIONAL GROWTH

The time rate of change of mass for an individual ice crystal denoted in Eq. (2.14) can be obtained from the classic mass growth theory, including the conservation of water mass and total energy at the ice crystal surface. The diffusional growth for an individual ice crystal can be expressed as follows:

$$\frac{dm}{dt} + 4\pi C' D' f_1 \Delta\rho = 0, \quad (2.17)$$

$$L_s \frac{dm}{dt} + H_R - 4\pi C' K' f_2 \Delta T = 0, \quad (2.18)$$

where m is the mass of an individual crystal; C' is the equivalent radius for diffusive processes of a nonspherical crystal; D' and K' are the diffusion coefficients for water vapor and heat, respectively; f_1 and f_2 are the combined ventilation and surface curvature factors, respectively; $\Delta\rho$ and ΔT are the density and temperature differences between the ice crystal and the environment, respectively; and H_R denotes the radiative effect on the individual ice crystal.

The analytic expressions for the mass growth rate and ice crystal temperature can be derived by solving Eqs.

(2.17) and (2.18) simultaneously. Moreover, using the Clausius–Clapeyron equation, the ideal gas law, and Kelvin's expression for vapor pressure, we obtain the following equation for ice crystal growth:

$$\frac{dm}{dt} = AS - BH_R, \qquad (2.19)$$

where

$$S = (s_i - 1) - \frac{2s}{\rho_i R_w T r}, \qquad (2.20)$$

$$A = \frac{4\pi f_2 K' C'}{B'}, \qquad (2.21)$$

$$B = \frac{L_s}{R_W T^2 B'}, \qquad (2.22)$$

$$B' = \frac{L_s^2}{R_W T^2} + \frac{f_2 K' R_W T}{f_1 D' e_s}, \qquad (2.23)$$

and s_i is the ice saturation ratio, s is the surface free energy of ice, ρ_i is the bulk ice density, T is temperature in kelvins, R_w is the gas constant for water, r is half of the ice crystal width, and e_s is the saturation vapor pressure with respect to ice at temperature T. The values for the unknown coefficients are taken from Laube and Holler (1988), Ramaswamy and Detwiler (1986), Heymsfield (1972), and Auer and Veal (1970). The coefficients defined in Eqs. (2.19)–(2.23) are listed in appendix B.

2) RADIATIVE EFFECTS

The heating due to radiation effect on the individual ice crystal must be the product of the absorption cross section and the net radiative flux density and can be expressed as follows:

$$H_R = \int_0^\infty \sigma_{a,\lambda}(m_i)[F_\lambda^+ + F_\lambda^- - 2\pi B_\lambda(T)]\, d\lambda$$

$$\cong \overline{\sigma_a}(m_i)[F^+ + F^- - 2\sigma T^4], \qquad (2.24)$$

where H_R is the rate of radiative energy gained by an individual particle and is determined separately for each size bin, F^+ and F^- are the upward and downward net radiative fluxes, and $B_\lambda(T)$ is the Planck function at temperature T. To simplify the calculations, we may use a mean absorption cross section of an ice crystal $\overline{\sigma_a}$, which can be obtained from

$$\overline{\sigma_a} = \sum_{i=1}^{I} \sigma_{a,i}/I, \qquad (2.25)$$

where I is the total number of the spectral bands in the parameterization, and $\sigma_{a,i}$ is the absorption cross section of an ice crystal for a given wavelength determined from the parameterization equations presented in Fu and Liou (1993).

The radiative flux within a volume element of cloud can be obtained from the radiation scheme described in section 2b. In this manner, the ice crystal size distribution is fully interactive with radiation via the ice crystal mean effective size and IWC.

3) TERMINAL VELOCITY

We follow the formula developed by Böhm (1989) for the terminal velocity of ice particles, given by

$$U_f = \frac{R_e \eta}{\rho L}, \qquad (2.26)$$

where η denotes the air viscosity; L is the ice crystal characteristic length, which can be computed from the empirical relationship given by Auer and Veal (1970); and R_e is the Reynold number, which can be calculated from the unified Davis number (Böhm 1989).

4) NUCLEATION

Ice nucleation processes can be generally classified in four modes: homogeneous freezing nucleation, heterogeneous freezing nucleation, heterogeneous deposition nucleation, and contact freezing nucleation. As Chen and Lamb (1994) pointed out, homogeneous freezing nucleation usually occurs at or below $-40°C$, while heterogeneous freezing is likely to be more effective when sufficient water is involved. Since the temperature in the present model ranges from $-20°$ to $-40°C$ and since no liquid water is considered, only heterogeneous deposition nucleation is included. The nucleation process requires the presence of ice nuclei (IN). Fletcher (1962) developed a relationship between the effective IN concentration and temperature as follows: $N_{IN} = N_0 \exp[b(T_{STD} - T)]$, where N_0 and b are constants, and $T_{STD} = 273.15$ K. This expression implies that N_{IN} is a well-defined function of temperature. However, Meyers et al. (1992) found that Fletcher's equation tends to underpredict ice crystal concentrations for temperatures warmer than $-20°C$, while overpredicting them for colder clouds. Gagin (1972) and Huffman (1973) found that the number concentration of effective IN increases with increasing supersaturation over ice S_i in the form

$$N_{IN} = cS_i^k, \qquad (2.27)$$

where c and k are constants determined from Huffman (1973) and Chen and Lamb (1994). Heterogeneous deposition nucleation is taken into account using this relationship. The effective INs nucleate immediately, implying that their appearance is the same as the creation of new ice particles. The nucleation process is assumed to be irreversible, that is, $dN_{IN} \geq 0$.

d. Boundary conditions and numerical methods

Cyclic boundary conditions are specified at the lateral boundaries. The upper and lower boundaries are set so
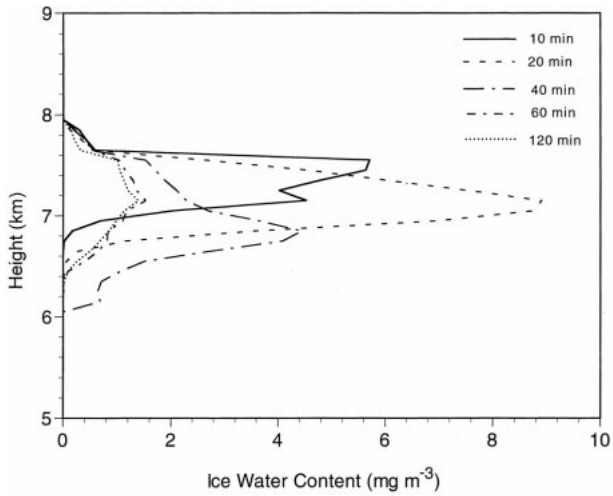
FIG. 1. Vertical profile of the horizontally averaged IWC simulated from the model at five time steps.

that the evolving disturbances remain isolated within the domain, that is,

$$\zeta = 0, \qquad \psi = 0, \quad \text{and} \qquad (2.28)$$

$$\frac{\partial \theta}{\partial t} = -w_0 \frac{\partial \theta_0}{\partial z}, \qquad \frac{\partial q}{\partial t} = w_0 \frac{\partial q_0}{\partial z}. \qquad (2.29)$$

No cross-boundary transport of perturbation quantities is allowed at the lower and upper boundaries such that

$$\frac{\partial \zeta}{\partial z} = \frac{\partial \theta}{\partial z} = \frac{\partial q}{\partial z} = 0. \qquad (2.30)$$

The second-order turbulence moments are simply set to zero.

The C grid presented by Arakawa and Lamb (1977) is used in the model, with dynamic quantities defined at grid points and thermodynamic variables defined at points offset by a one-half grid interval in both the x and z directions. The horizontal turbulent fluxes are located at the physical lateral boundaries, while the vertical turbulent fluxes are located at the physical upper and lower boundaries following Krueger (1988). The model domain covers 3 km in the vertical and 6 km in the horizontal with a uniform horizontal and vertical grid spacing of 100 m. To test if this grid spacing is sufficient to resolve the cloud cluster, we have carried out a simulation in which the spacing is reduced to 50 m. The mean profiles of the basic variables obtained from the simulations using these two resolutions are substantially the same. Thus, the former has been used in the presentation of results. The nonlinear term of the vorticity equation (2.8) is evaluated by the finite-difference scheme in terms of the flux form using Arakawa's (1966) nine-point Jacobian, which conserves both the mean kinetic energy and mean square vorticity. The nonlinear terms in Eqs. (2.9) and (2.10) are computed following the method developed by Lilly (1965). The turbulence equations also contain a number of nonlinear terms in which the simplest centered difference forms are employed. Equations (2.8)–(2.10) are solved by using the second-order Adams–Bashforth scheme, except that the Euler forward scheme is used for the initial time step. The Euler forward scheme is also adopted for the solution of ice crystal size distributions denoted in Eq. (2.11).
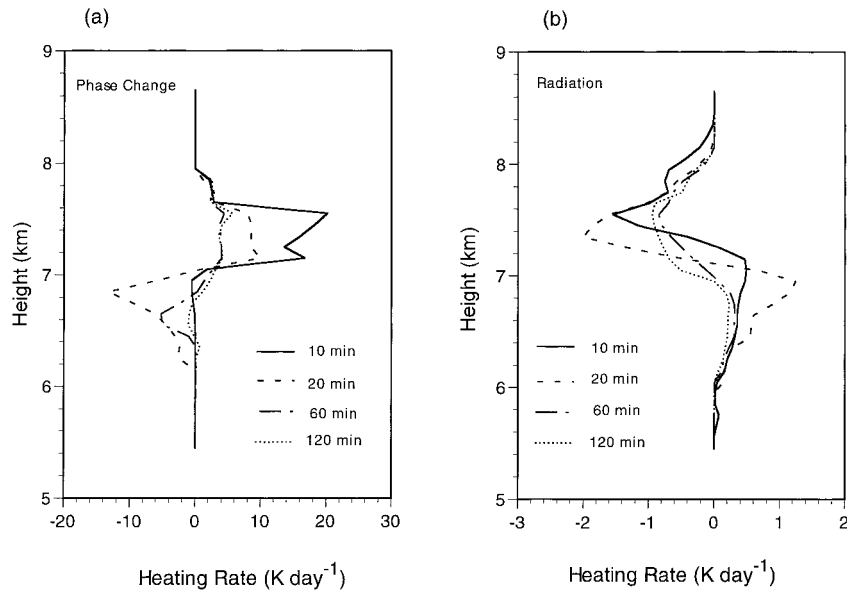

FIG. 2. Vertical profiles of the horizontally averaged heating rates due to (a) phase change and (b) radiation at four time steps.
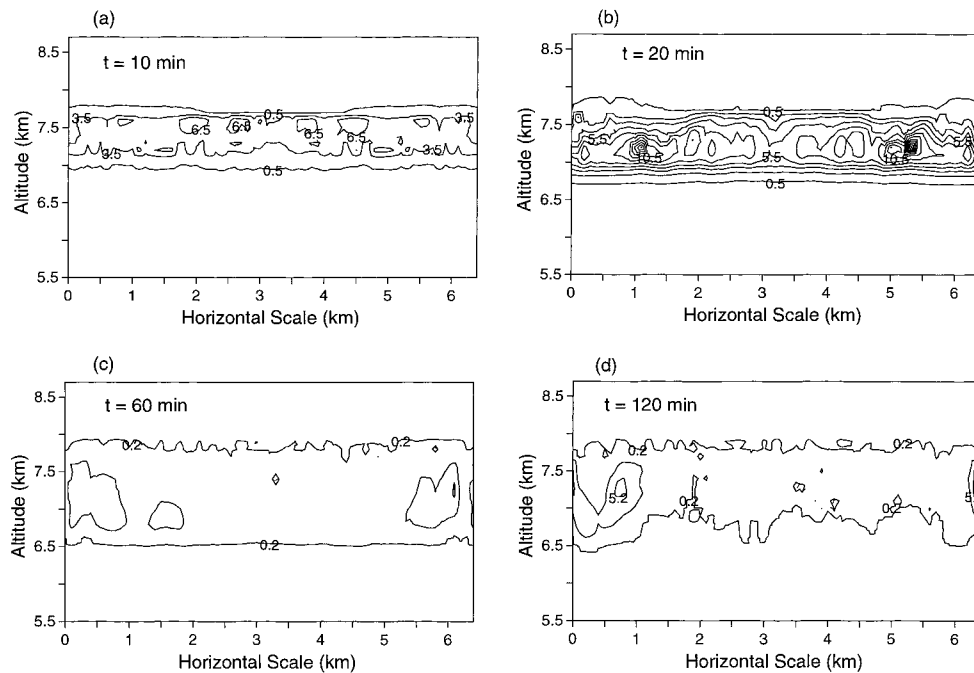
FIG. 3. Contour maps of IWC (mg m^{-3}) at four time steps. (a) $t = 10$ min, (b) $t = 20$ min, (c) $t = 60$ min, and (d) $t = 120$ min.

3. Simulation results

a. Initial condition

To investigate the physical interaction of radiation, ice microphysics, and turbulence in the life cycle of cirrus clouds, we have performed a number of simulations involving the formation and evolution of a thin cirrus cloud. The initial thermal stratifications used in the present model are a number of specified lapse rates
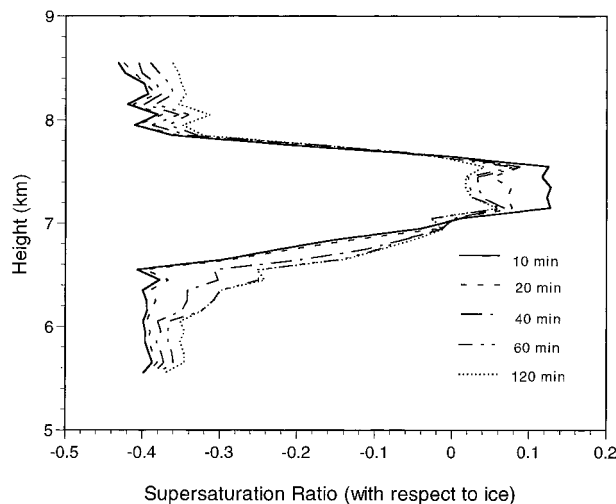
FIG. 4. The vertical profile of the horizontally averaged supersaturation ratio with respect to ice at five time steps.

in various vertical regions, which are expressed in terms of the pseudoadiabatic lapse rate governing the unmixed vertical displacements at ice saturation, typical of thin cirrus cloud layers. The lapse rates of 7.2°, 8.7° (which corresponds to the pseudoadiabatic lapse rate governing unmixed convection at ice saturation), and 4.7°C km^{-1} are set below 6.95 km, between 6.95 and 7.55 km, and above 7.55 km, respectively. The temperature ranges from $-20°$ to $-40°$C. The relative humidity with respect to ice is set at 115% in the initial cloud generation region (6.55–7.55 km), and 60% otherwise. The initial state is horizontally uniform and at rest, except for the large-scale vertical motion that is related to the dynamic forcing and is prescribed as a constant with a value of 2 cm s^{-1}. There is no ice water initially. The mean spring *U.S. Standard Atmosphere, 1976,* is used outside the model domain for initialization of the radiative transfer scheme. The solar zenith angle is calculated from the geometric relationship involving the latitude (40°N), the time of the year (18 March), and the local solar time (1300 LST). The disturbance is initiated through the prescribed potential temperature perturbations at all grid points covering the layer from 6.55 to 7.55 km, with a maximum and a mean value of 0.1° and 0.05°C, respectively. Both positive and negative perturbations occur in this region.

b. Cirrus cloud simulation results

Figure 1 shows the vertical profile of the horizontally averaged IWC ($\overline{\text{IWC}}$) during a 120-min cirrus
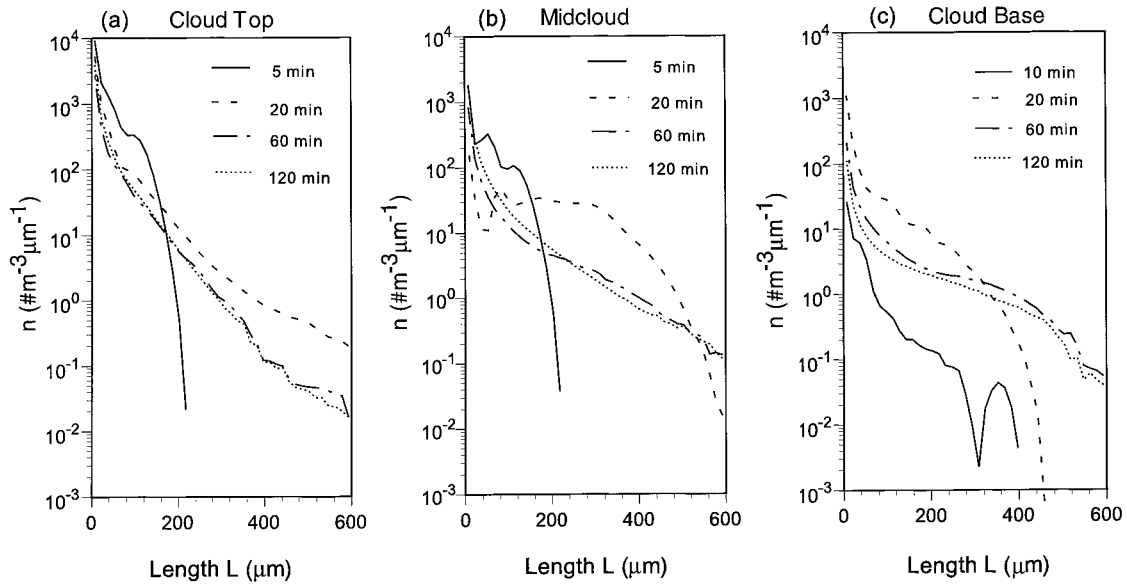
FIG. 5. Ice crystal size distributions at different altitudes: (a) cloud top, (b) midcloud, and (c) cloud base, at four time steps.

cloud simulation. Ice crystals form initially by the deposition nucleation associated with the saturated air produced by dynamic and thermodynamic forcings. At $t = 10$ min, $\overline{\text{IWC}}$ increases from 0 to about 5.7 mg m^{-3}. The nucleation process stops when the supersaturation ratio begins to decrease due to deposition. Ice crystals are then subject to diffusional growth, advection, sedimentation, and eddy diffusion. Ice crystals become larger and fall to lower levels. At $t = 20$ min, $\overline{\text{IWC}}$ reaches its maximum value of about 9 mg m^{-3}, and the location of its maximum shifts from 7.55 km at $t = 10$ min to 7.15 km at $t = 20$ min. At the same time, the cloud base is moving downward. After ice crystals fall into the drier lower region, sublimation occurs and the simulated maximum $\overline{\text{IWC}}$ decreases to about 4.2 mg m^{-3} at $t = 40$ min. After $t = 60$ min, a near steady state is reached. Observations of cirrus IWC in weak synoptic forcing situations have been reported to be between 3 and 8 mg m^{-3} over a horizontal path longer than 3 km and with a temperature range of $-30°$--$-40°$C (Heymsfield 1975). The present model results thus appear to compare reasonably with these previous observations.

The updrafts in the cloud layer are larger than the downdrafts in the earlier stage of the simulation, with maximum values of about 30 and 5 cm s^{-1}, respectively, at $t = 20$ min. Toward the end of the simulation, updrafts and downdrafts are of the same magnitude with a value of about 15 cm s^{-1}. The simulation results are comparable to the observed vertical velocities in cirrostratus, with typical values ranging from 5 to 20 cm s^{-1} and a maximum of about 60 cm s^{-1} (Heymsfield 1977).

The ice water formation processes can also be illustrated from the vertical profiles of heating rate associ-

ated with the phase change of ice and radiation at different time steps as shown in Fig. 2. In the cloud generation region, temperature increases because latent heat is released by the formation and growth of ice crystals. In the lower region where the air is not saturated, however, ice particles sublimate and temperature decreases. Thus, by the release of latent heat, the upper part of the cloud is heated and the lower part is cooled, resulting in the increase of stability (Fig. 2a). Net radiative cooling occurs in the upper part of the cloud, whereas heating takes place in the subcloud region, implying that radiation plays an active role in decreasing cloud stability. The preceding radiation and latent heat effects on cloud stability during cirrus cloud evolution are in line with those presented in Starr and Cox (1985). The horizontally averaged IR cooling rate is negative throughout the cloud with a maximum of about $-3.6°$C day^{-1} at the cloud top, whereas the solar heating rate is positive, having a maximum of about 3°C day^{-1} in the middle part of the cloud. These results, while smaller than those obtained from the models using bulk microphysics parameterizations (e.g., Starr and Cox 1985; Gu and Liou 1997a,b), are in good agreement with the values reported by Khvorostyanov and Sassen (1998b), who also used an explicit microphysics module in the cirrus cloud model. Finally, it should be noted that heating due to the turbulent transport is negative in the cloud generation region and is positive in the subcloud region. Contribution from this term, however, is much smaller than that from phase change and radiation terms by about two orders of magnitude.

Distributions of the simulated IWC at four time steps are shown in Fig. 3. In the calculation of IWC, the minimum number density is assumed to be a small value

of 1 m^{-3} in order to obtain the maximum possible contribution of ice crystals. Usually the significance of the total ice crystal number density becomes negligible when its value is less than about 10 m^{-3} or even larger. Zhang et al. (1989), for example, used 50 m^{-3} as the minimum number density in their simulation study, and a value of about 10^{-2} was obtained in terms of the ice crystal size distribution (m^{-3} μm^{-1}). As shown in Fig. 3, some small cells are observed around 7.4 km at t = 10 min. At t = 20 min, the maximum simulated IWC is located at about 7.2 km with a value of about 20 mg m^{-3}, which is close to that reported by Heymsfield (1975). The cells become vertically elongated with time, similar to the results presented by Starr and Cox (1985). The cloud base moves from 6.8 km initially to about 6.4 km at the end of the simulation as a result of the relative fall speed of ice crystals and the weakening of updrafts during the cloud's evolution. Overall, the foregoing results are in general agreement with those obtained from the 2D cirrus cloud model that uses parameterizations to account for the phase change of ice and the vertical flux of ice water (Gu and Liou 1997a,b). The main difference, however, is that IWC increases to its maximum value much faster in the parameterized scheme in which the total excess water vapor is deposited to ice water immediately in one time step and the depletion of water vapor by diffusional growth after the formation of ice crystals is not taken into account. This result is in agreement with the conclusion presented in Khvorostyanov and Sassen (1998b) that the ice crystal phase relaxation time takes about 0.5–2.0 h.

Figure 4 illustrates the time-dependent evolution of the supersaturation ratio, which decreases with time in the cloud formation layer but increases in the sublimation region below. It is clear that in the region where water vapor is deposited to ice crystals, water vapor in the ambient air is diminishing and thus the saturation ratio decreases. When ice particles are sublimating, water vapor is released and the saturation ratio increases. At the same time, the ice crystal sedimentation process transports ice into the sublimation region where it serves as a moisture source. Note that the supersaturation ratio decreases slowly after t = 40 min and is still slightly positive after t = 60 min. This again demonstrates the difference between the explicit ice microphysics and parameterization schemes. In the latter, the excess water vapor is depleted into ice water immediately at the beginning of the simulation, with the corresponding maximum IWC reached as early as t = 5 min (Starr and Cox 1985).

The evolution of ice particle size distribution at different altitudes is displayed in Fig. 5. Ice crystals are first formed by nucleation and subsequently grow through diffusional growth. The size distribution changes as a result of the diffusional growth, advection, sedimentation, and turbulence processes. At t = 5 min, the maximum ice crystal size is about 200 μm at the cloud top of 7.55 km. At t = 10 min, the number
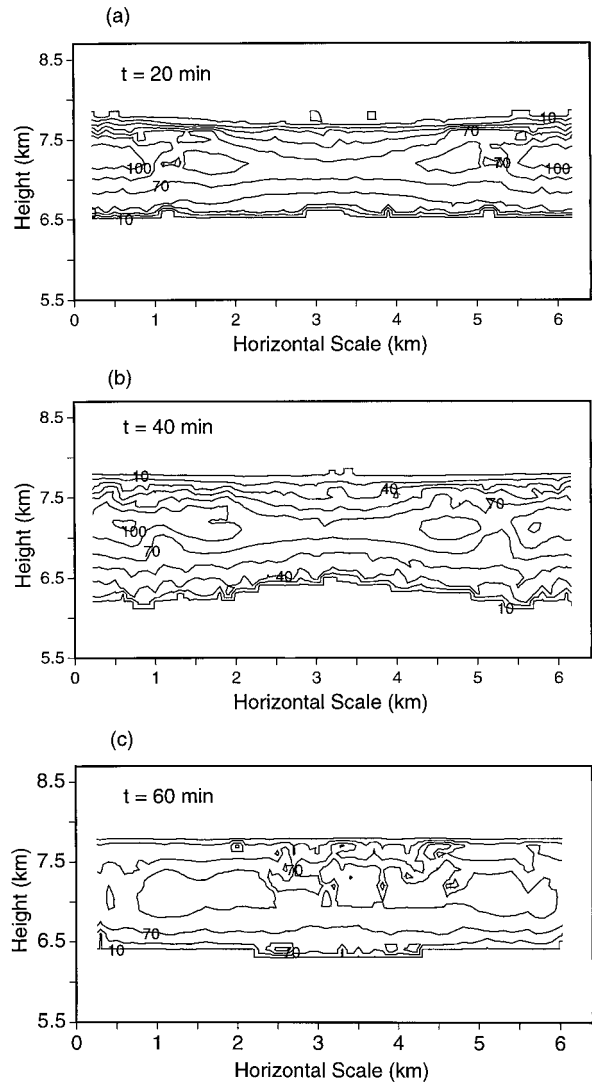

FIG. 6. Distributions of the mean effective ice crystal size (μm) at three time steps: (a) t = 20 min, (b) t = 40 min, and (c) t = 60 min.

densities of ice crystals with sizes smaller than 300 μm have the largest values and decrease after this time period. Ice crystals grow continuously and the largest one of about 600 μm is generated at t = 20 min when the IWC reaches its maximum value. After t = 20 min, the number densities of larger ice crystals are reduced because they fall to the lower level, while those of smaller ice particles remain almost unchanged. The ice crystal size distributions reach a near steady state after t = 40 min (Fig. 5a). Figure 5b shows the time-dependent evolution of the ice crystal size distribution at 7.15 km, corresponding to the middle of the cloud. The number densities of small ice crystals here are much less than those at higher altitudes, while those of larger ice particles are roughly comparable after t = 20 min. The number densities
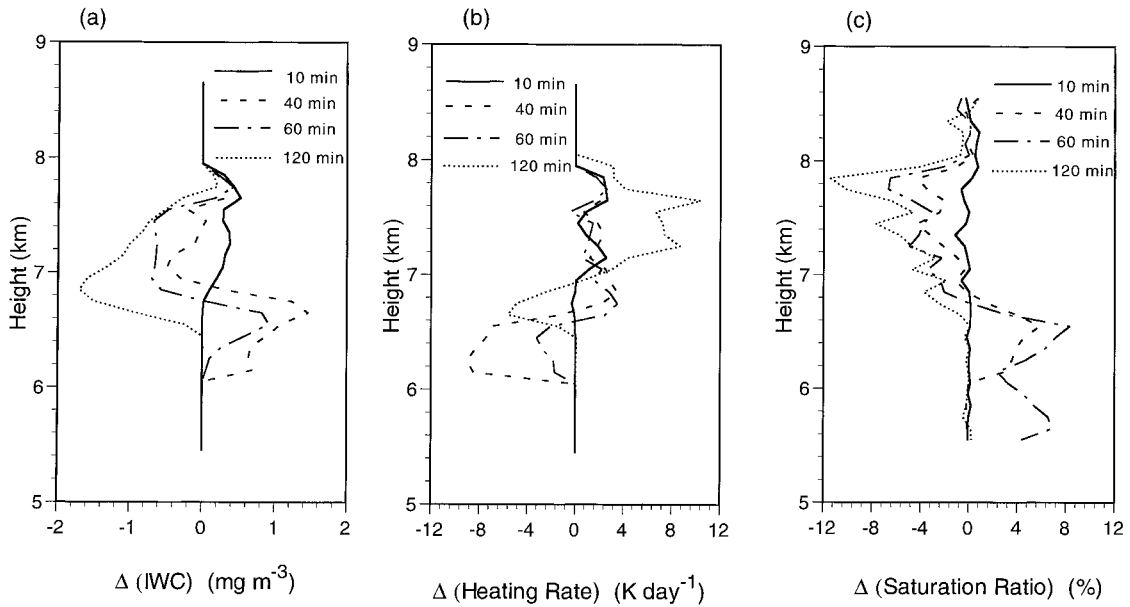
FIG. 7. Differences (with radiation minus without radiation) of the vertical profiles of the horizontally averaged (a) IWC, (b) the heating rate due to phase change, and (c) the saturation ratio at four time steps.

of ice crystals smaller than 500 μm reach their maximum values at $t = 20$ min. These ice crystal numbers then decrease due to sublimation in favor of the growth of larger particles. The largest ice particle size is about 600 μm after $t = 40$ min. At 6.75 km (near the cloud bottom), no ice crystal is formed initially.

At $t = 10$ min, the largest ice crystal size there is about 400 μm. The number densities of large ice crystals then increase rapidly after $t = 20$ min. This, again, is because larger ice crystals have greater terminal velocities and fall more rapidly to the lower level (Fig. 5c). The ice crystal size distributions at the middle
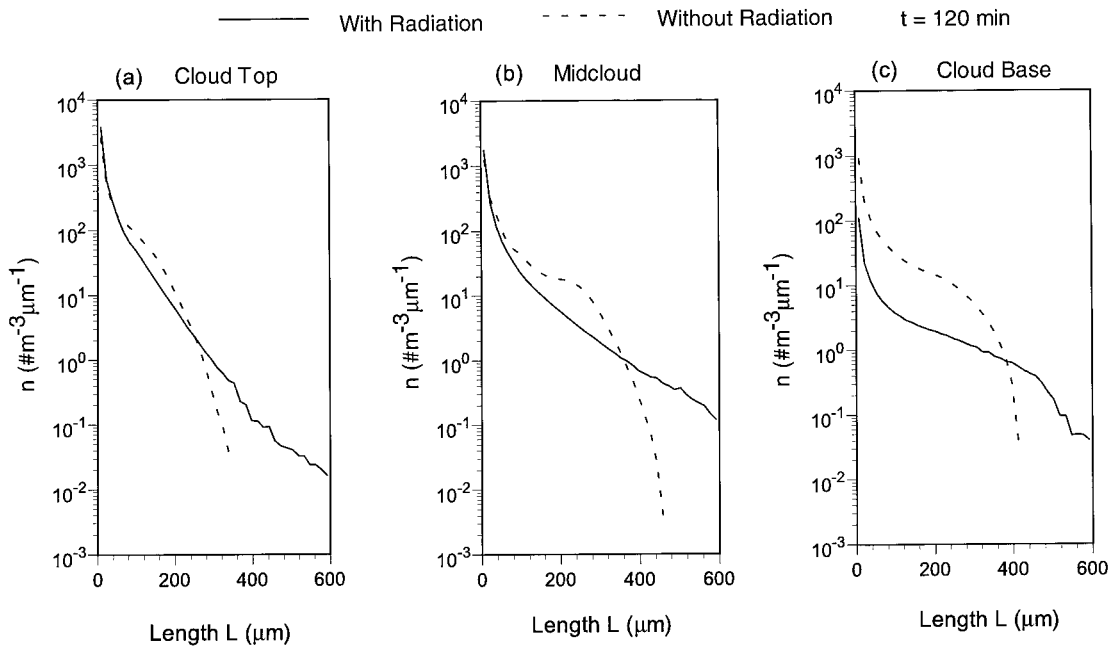

FIG. 8. Ice crystal size distributions at different altitudes: (a) cloud top, (b) midcloud, and (c) cloud base, at $t = 120$ min for simulations with (solid) and without (dashed) radiation.
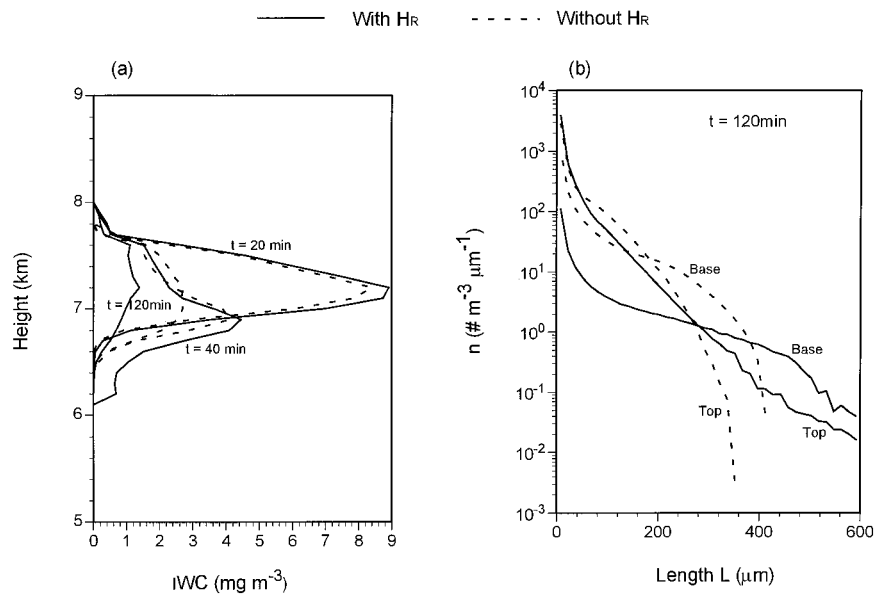
FIG. 9. (a) Vertical profile of the horizontally averaged IWC at three time steps and (b) ice crystal size distributions at cloud top and bottom at $t = 120$ min for simulations with (solid) and without (dashed) including the radiation effect in the diffusional growth of ice crystals.

and lower parts of the cloud reach a near steady state after $t = 60$ min.

Figure 5 also illustrates the temporal and spatial variabilities of ice crystal size distributions simulated by the model. At $t = 5$ min, no ice crystal is formed below the supersaturated level. Ice crystals grow and fall to the lower region. Finally, ice crystals smaller than 300 μm dominate at the cloud top, while larger particles are located mainly at lower levels. These size distributions are in general agreement with the ice crystal size distributions collected during FIRE II Intense Field Observation (IFO) and analyzed by Ou et al. (1995), as well as those presented by Heymsfield and Platt (1984). For the temperature range from $-20°$ to $-40°$C, observations of the average size spectra show that the number densities tend to increase with decreasing temperature for small particles, while they decrease with decreasing temperature for large particles. In the present model, the lower parts of the cloud have higher temperatures and possess higher number densities of large ice particles. The cloud top, on the other hand, is cooler and shows the presence of more small ice particles.

Figure 6 shows the mean effective ice crystal sizes over the model domain at 20, 40, and 60 min. These sizes range from 0 to 120 μm and are in general agreement with those determined from the FIRE II IFO data reported by Ou et al. (1995). The mean effective ice crystal sizes determined from both replicator data and satellite retrieval for a number of carefully selected cirrus cloud cases were mostly between 40 and 100 μm. The location of the maximum ice crystal size and the

cloud base simulated from the model moves downward with time.

c. Radiation effects in cirrus cloud evolution

Vertical profiles of the differences of $\overline{\text{IWC}}$, latent heat, and the saturation ratio at four time steps between simulations with and without radiation are shown in Fig. 7. Inclusion of the radiation effect enhances the latent heat release in the cloud generation region after $t = 10$ min, implying that the deposition and hence the rate of net formation are enhanced. Moreover, the sublimation process in the lower area is also strengthened after $t = 40$ min. The corresponding supersaturation ratio decreases (increases) in the cloud formation region (the region below) due to radiation effects, revealing that radiation enhances both deposition and sublimation. Evidently, radiation appears to enhance stability during the maintenance and dissipation periods of the cirrus cloud evolution. The simulated $\overline{\text{IWC}}$ is also larger during the cloud formation period when radiation is included. However, less $\overline{\text{IWC}}$ occurs in the cloud generation region after $t = 40$ min with radiative processes included in the model. This surprising result may be explained by the effects of radiation on ice crystal growth as detailed in the following.

Figure 8 presents the details of radiation effects on the ice crystal size distributions. Radiative cooling tends to increase the number densities of larger ice crystals. This can be explained from Eq. (2.14), in which radiative cooling contributes to the growth of ice crystals. Larger ice crystals and corresponding larger fall speeds

result in less $\overline{\text{IWC}}$ in the cloud generation region, but more in the subcloud region during the maintenance period (Fig. 7a). The sublimation process is also strengthened by radiative effects, leading to smaller number densities of ice crystals with sizes less than 300 μm in the subcloud region after $t = 40$ min. Because more sublimation occurs when radiation is included at $t = 40$ min, the corresponding $\overline{\text{IWC}}$ becomes less after $t = 60$ min (Fig. 7a). The ranges of size spectra become narrower when radiation is not included in the model. Similar results have also been reported by Zhang et al. (1989).

The effects of radiation on the diffusional growth of individual ice crystals are illustrated in Fig. 9. Radiative cooling significantly enhances the production of large ice crystals at the cloud top, but the production is decreased by heating in the level below. Clearly, radiation plays an important role in the ice crystal growth process and hence substantially modulates the ice crystal size distributions (Fig. 9b). According to the diffusional growth equation, when radiative cooling is present at the cloud top (i.e., $H_R < 0$), the radiation effect contributes more significantly to the diffusional growth of ice crystals with larger cross sections. The cloud-scale updraft speeds with a maximum value of about 15 cm s^{-1} are now smaller than the fall speed of larger ice crystals. These ice crystals then fall to the lower drier level where the diffusional mass growth becomes negative because subsaturation occurs. The radiative heating in the lower part of the cloud then tends to strengthen the sublimation process. The simulated IWCs are larger before $t = 40$ min but smaller after $t = 60$ min when the radiation effect on individual ice crystals is taken into account in diffusional growth (Fig. 9a). It appears that this effect is significant when ice crystal size distributions are explicitly simulated in cirrus cloud models.

d. Role of turbulence in cirrus cloud evolution

The primary role of turbulence-scale turbulence is to modulate the supersaturation condition, which affects the rate of phase change between water vapor and ice crystals. Thus turbulence can interact with radiation by enhancing the net cooling rate and by increasing the radiative destabilization (Gu and Liou 1997a,b). Figure 10 depicts the horizontally averaged vertical component of the turbulent kinetic energy at $t = 90$ min. A maximum value is shown in the upper part of the cloud with a magnitude of about one-third of the vertical component of the cloud-scale kinetic energy. The buoyancy flux produced by cloud-scale drafts is negative at the cloud top and positive within the cloud. The turbulence-scale buoyancy flux is comparable in value but opposite in sign. Turbulence tends to generate upward (downward) buoyancy flux in the upper (lower) part of the cloud and redistribute water vapor within the cloud. Cloud-scale drafts, on the other hand, mainly transport water vapor downward within the cloud, which may slow down the cloud formation process.
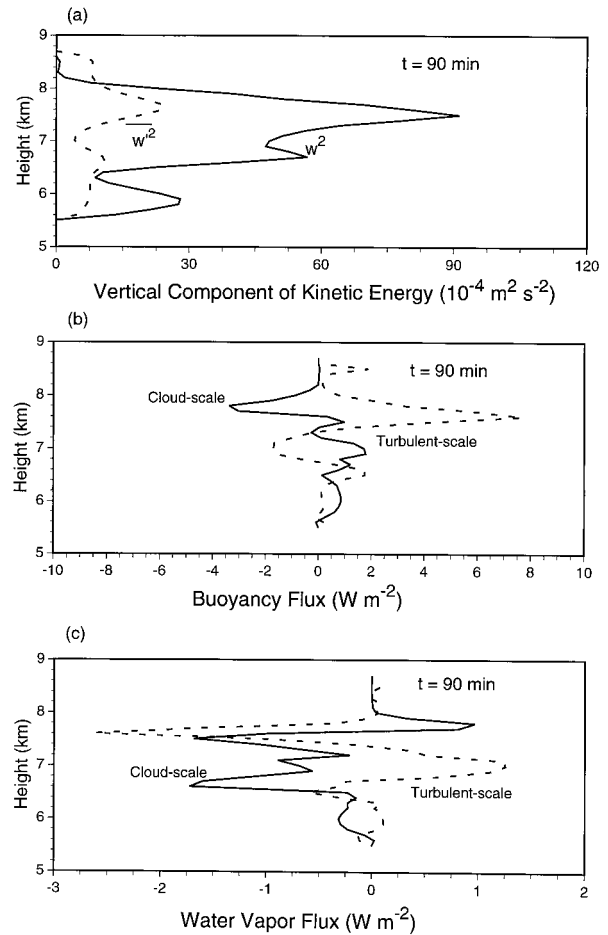

FIG. 10. Vertical profiles of the horizontally averaged cloud-scale (solid) and turbulence-scale (dashed) (a) vertical component of kinetic energy, (b) buoyancy flux, and (c) water vapor flux at $t = 90$ min.

Simulation without turbulence-scale turbulence has also been carried out to examine the role of turbulence in the evolution of cirrus clouds. Turbulence-scale turbulence normally provides smoothing effects in the model. To prevent the growth of numerical instabilities when turbulence closure is turned off, we have included a very small fourth-order damping term in each prognostic equation, which is small enough not to affect the resolvable variables, following Klemp and Wilhelmson (1978). The direct effect of turbulence on the ice crystal size distributions is shown in Fig. 11. After $t = 40$ min, the action of turbulence leads to the generation of more intermediate to large ice crystals ($L > 200$ μm), especially in the middle and lower parts of the cloud. The corresponding time-dependent behavior of the domain-averaged IWC also shows substantial differences after $t = 40$ min, revealing that turbulence is likely to be more important in the maintenance and dissipation stages. The heating rates due to latent heat release during
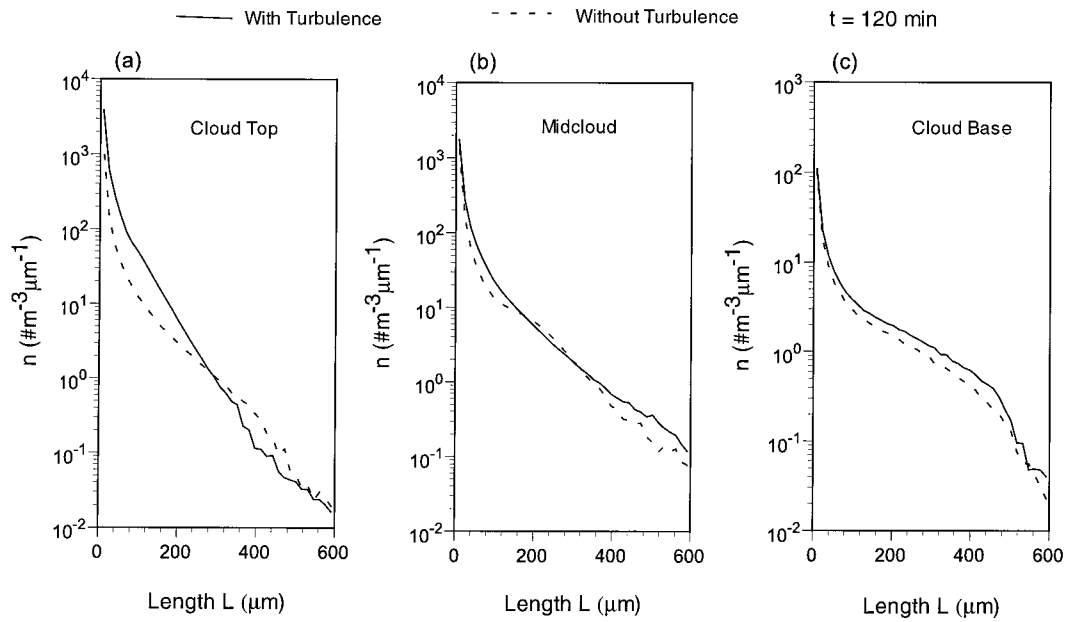
FIG. 11. Ice crystal size distributions at different altitudes: (a) cloud top, (b) midcloud, and (c) cloud base, at $t = 120$ min for simulations with (solid) and without (dashed) turbulence-scale turbulence.

this period indicate that turbulence enhances both deposition in the cloud generation region and sublimation in the region below. The effects of turbulence closure in the cirrus cloud model are further examined in the following.

Figure 12 shows the differences (second-order results minus first-order results) in saturation ratio and the heating rate associated with phase change averaged over a time period of 60–90 min between second- and first-order closures. Use of the second-order turbulence closure appears to enhance the latent heat release within the cloud and decrease the stability in the lower region. Starr and Cox (1985) stated that occurrence of a second convectively active region below the initial cloud layer is very common, which may lead to the formation of multilayered thin cirrus. Turbulence appears to play an important role in this process, as is evident from the incorporation of second-order closure that reduces low-
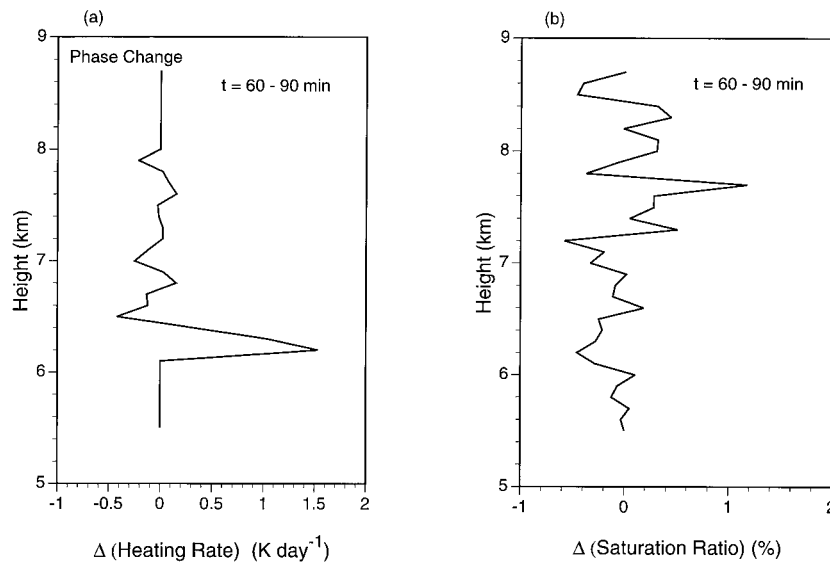

FIG. 12. Differences averaged over a period of 60–90 min for (a) the heating rate due to phase change and (b) the saturation ratio between simulations using second-order and first-order turbulence closures (second-order minus first-order) in the cloud model.

er-level stability. The saturation ratio decreases at the cloud top but increases above the cloud, implying that more moisture is transported to higher levels when the second-order closure is employed.

4. Summary

A 2D time-dependent numerical model focusing on cloud-scale processes with a grid resolution of 100 m has been developed to investigate the interaction among radiative processes, turbulence, and ice microphysics, and their effects on the formation of cirrus clouds. The new features of the model include a radiation scheme that interacts with the ice crystal size distribution via IWC and a mean effective ice crystal size, the effect of radiation on the growth of individual ice crystals, and a second-order closure for turbulence. Large-scale dynamic forcing is taken into account through an initial large-scale vertical motion. The ice microphysical properties are determined by nucleation, diffusional growth, horizontal and vertical advection, sedimentation, and eddy diffusion. The ice crystal lengths are divided into a finite number of bins in the simulation of ice crystal size distributions.

Numerical results show that ice crystals form initially by nucleation associated with the saturated air and the dynamic and thermodynamic forcings. Subsequently, they grow by means of the diffusional growth process, advection, gravitational sedimentation, and turbulence. Radiative processes begin to play an important role once a sufficient amount of ice water is produced in the atmosphere. Radiative cooling provides an impetus to the growth of ice crystals at the cloud top through its effect on individual ice crystals, while radiative heating enhances the sublimation of ice crystals in the lower region. Radiatively forced processes play an important role during the evolution of ice crystal size distributions. The action of radiative heating and cooling increases the number densities of large ice particles but reduces those of the small ones in the lower level. When radiative properties are included in the model, larger ice crystals and larger fall speeds lead to less ice in the cloud generation region. The simulated size spectra become narrower when radiation is not included in the model. Since cirrus is not opaque, radiative cooling or heating is distributed within the entire cloud. Consequently, radiatively driven convection is closely associated with the ice mass vertical distribution. The effects of the magnitude of radiative heating rates and the locations of the cloud top and base in the present cirrus cloud case are smaller than those in the radiatively driven stratiform cloud. The induced turbulence-scale turbulence begins to play a substantial role in the evolution of cirrus soon after the effects of radiation become significant. Turbulence affects the phase changes of ice and the formation of ice crystal size distributions. Differences in the simulation results between the use of second- and first-order turbulence closures show that turbulence effects are more vigorous when the former is used in the model, resulting in enhanced instability and more moisture being transported to higher levels.

As shown in the preceding presentation, radiative fluxes and heating rates play important roles in the evolution of cirrus clouds. Radiation calculations involving clouds in this model have been carried out by using the plane-parallel assumption on a column-by-column basis. It is clear from the model simulation of IWC and ice crystal size distribution that cirrus clouds are highly inhomogeneous and finite in extent. How would the horizontal radiative flux exchanges affect the growth of ice crystals? It is our intent to investigate the cloud inhomogeneity effects on the distribution of radiative fluxes and heating rates and their feedback to ice microphysical properties and dynamic fields in a cirrus cloud model by using an appropriate 3D radiative transfer model for inhomogeneous clouds.

APPENDIX A

The Second-Order Turbulence Closure

A second-order turbulence closure is developed and incorporated in the present cirrus cloud model. We follow the level-4 closure model developed by Mellor and Yamada (1974) and further apply the assumptions made for the potential temperature to the moisture field. The mean Reynolds stress model equations for the calculation of the evolution of turbulent fluxes can be written in the forms

$$\frac{\partial \overline{u_i' u_j'}}{\partial t} - \frac{\partial}{\partial x_k}\left[E\lambda_1 \left(\frac{\partial \overline{u_i' u_j'}}{\partial x_k} + \frac{\partial \overline{u_i' u_k'}}{\partial x_j} + \frac{\partial \overline{u_j' u_k'}}{\partial x_i} \right) \right] = -\overline{u_k' u_i'}\frac{\partial u_j}{\partial x_k} - \overline{u_k' u_j'}\frac{\partial u_i}{\partial x_k} - \frac{2}{3}\frac{E^3}{\wedge_1}\delta_{ij} - \frac{E}{3\ell_1}\left(\overline{u_i' u_j'} - \frac{\delta_{ij}}{3}E^2 \right) + c_1' E^2 \left(\frac{\partial u_i}{\partial x_j} + \frac{\partial u_j}{\partial x_i} \right)$$
$$- \beta(g_j \overline{u_i'\theta'} + g_i \overline{u_j'\theta'}) + c_2'\beta\left(g_j \overline{u_i'\theta'} + g_i \overline{u_j'\theta'} - \frac{2}{3}\delta_{ij}g_k \overline{u_k'\theta'} \right), \quad (A.1)$$

$$\frac{\partial \overline{\theta'^2}}{\partial t} - \frac{\partial}{\partial x_k}\left(E\lambda_2 \frac{\partial \overline{\theta'^2}}{\partial x_k} \right) = -2\overline{u_k'\theta'}\frac{\partial \theta}{\partial x_k} - 2\frac{E}{\wedge_2}\overline{\theta'^2}, \quad (A.2)$$

$$\frac{\partial \overline{u_j'\theta'}}{\partial t} - \frac{\partial}{\partial x_k}\left[E\lambda_3 \left(\frac{\partial \overline{u_j'\theta'}}{\partial x_k} + \frac{\partial \overline{u_k'\theta'}}{\partial x_j} \right) \right] = -\overline{u_j'u_k'}\frac{\partial \theta}{\partial x_k} - \overline{u_k'\theta'}\frac{\partial u_j}{\partial x_k} - \beta g_j \overline{\theta'^2} - \frac{E}{3\ell_2}\overline{u_j'\theta'} + c_3' g_j \beta \overline{\theta'^2}, \quad (A.3)$$

$$\frac{\partial \overline{q'^2}}{\partial t} - \frac{\partial}{\partial x_k}\left(E\lambda_2 \frac{\partial \overline{q'^2}}{\partial x_k} \right) = -2\overline{u_k'q'}\frac{\partial q}{\partial x_k} - 2\frac{E}{\wedge_2}\overline{q'^2}, \quad (A.4)$$

$$\frac{\partial \overline{u_j'q'}}{\partial t} - \frac{\partial}{\partial x_k}\left[E\lambda_3 \left(\frac{\partial \overline{u_j'q'}}{\partial x_k} + \frac{\partial \overline{u_k'q'}}{\partial x_j} \right) \right] = -\overline{u_j'u_k'}\frac{\partial q}{\partial x_k} - \overline{u_k'q'}\frac{\partial u_j}{\partial x_k} - \beta g_j \overline{q'\theta'} - \frac{E}{3\ell_2}\overline{u_j'q'} + c_3' g_j \beta \overline{q'\theta'}, \quad (A.5)$$

$$\frac{\partial \overline{q'\theta'}}{\partial t} - \frac{\partial}{\partial x_k}\left(E\lambda_2 \frac{\partial \overline{q'\theta'}}{\partial x_k} \right) = -\overline{u_k'\theta'}\frac{\partial q}{\partial x_k} - \overline{u_k'q'}\frac{\partial \theta}{\partial x_k} - 2\frac{E}{\wedge_2}\overline{q'\theta'}. \quad (A.6)$$

Equation (A.1) contains prognostic equations involving the turbulent kinetic energy components and the turbulent fluxes of momentum. Equation (A.3) includes equations for the turbulent fluxes of potential temperature, while (A.5) for moisture turbulent fluxes. In these equations, β is the coefficient of thermal expansion; $g_j = (0, 0, -g)$ is the gravity vector; E is the square root of twice the turbulence kinetic energy; c_1', c_2', and c_3' are constants taken from Mellor and Yamada (1974); and λ_1, λ_2, λ_3, l_1, l_2, and $\wedge_1$, $\wedge_2$ are all length parameters that are related to the turbulent length scale l, which is proportional to the size of the largest turbulent eddies. Since they are confined to the turbulent region, l is related to the mixed-layer depth. For the length scale, we have adopted the interpolation formula given by Blackadar (1962) in the form

$$\ell = \frac{\kappa z}{1 + \kappa z/\ell_\infty}, \quad (A.7)$$

which interpolates between two limits $l \sim \kappa z$ as $z \to 0$ and $l \sim l_\infty$ as $z \to \infty$, with κ the von Kármán constant. Various propositions for l_∞ have been suggested in the literature. Following Bougeault (1981) we set $l_\infty = 0.15H$, with H the mixed-layer depth. Studies by Krueger and Bergeron (1994) on the sensitivity of the cumulus ensemble model to the turbulent length scale showed that a constant or uniform value for H should be used if Blackadar's formula is employed. We have set $H = 800$ m in this study. Finally, it should be pointed out that the first-order exchange concept has been used for ice crystal number density in the prognostic equation. Thus, second-moment terms associated with phase change have been neglected due in part to the lack of physical foundation.

REFERENCES

Arakawa, A., 1966: Computational design for long-term numerical integration of the equations of fluid motion: Two dimensional incompressible flow. Part I. *J. Comput. Phys.,* **1,** 119–143.
——, and V. R. Lamb, 1977: Computational design of the basic dynamical processes of the UCLA general circulation model. *Methods Comput. Phys.,* **17,** 174–265.
Auer, A. H., Jr., and D. L. Veal, 1970: The dimension of ice crystals in natural clouds. *J. Atmos. Sci.,* **27,** 919–926.
Baker, M. B., and J. Latham, 1979: The evolution of the droplet spectra and the rate of production of embryonic raindrops in small cumulus clouds. *J. Atmos. Sci.,* **36,** 1612–1615.

APPENDIX B

Values or Expressions Appearing in Eqs. (2.19)–(2.23)

Name of parameter	Symbol (unit)	Values or expressions
Capacity of the ice crystal	C' (m)	shape dependent
Gas kinetic efficiency of mass transfer	D' (m^2 s^{-1})	$\dfrac{D_v}{\dfrac{R_s}{R_s + \delta} + \dfrac{D_v f_1}{R_s \alpha_d}\left(\dfrac{2\pi}{R_w T}\right)^{1/2}}$
Diffusivity of water vapor in air	D_v (m^2 s^{-1})	$0.211\left(\dfrac{T}{273.2}\right)^{1.94}\dfrac{1013.3}{p} \times 10^{-4}$
Ventilation coefficient for mass diffusion	f_1	$1.0 + 0.14X^2, \quad X = N_{Sc}^{1/3}N_{Re}^{1/2} < 1$ $0.86 + 0.28X, \quad X \geq 1$
Gas kinetic efficiency of heat transfer	K' (J m^{-1} s^{-1} K^{-1})	$\dfrac{K_a}{\dfrac{R_s}{R_s + \delta} + \dfrac{K_a f_2}{R_s \alpha_T \rho_a c_p}\left(\dfrac{2\pi}{R_w T}\right)^{1/2}}$
Thermal diffusivity for dry air	K_a (J m^{-1} s^{-1} K^{-1})	$0.024 + 8 \times 10^{-5}T$
Ventilation coefficient for heat diffusion	f_2	$1.0 + 0.14X^2, \quad X = N_{Pr}^{1/3}N_{Re}^{1/2} < 1$ $0.86 + 0.28X, \quad X \geq 1$
Radius of ice crystal	R_s (m)	—
Jump distance	δ (m)	$4.62\dfrac{1013.3}{p}\dfrac{T}{293.15} \times 10^{-8}$
Deposition coefficient	α_d	0.1
Thermal accommodation coefficient	α_T	1.0
Schmidt number	N_{Sc}	$\dfrac{\eta}{\rho_a D_v} \approx 0.63$
Prandtl number	N_{Pr}	$\dfrac{\eta c_p}{K_a} \approx 0.72$
Reynolds number	N_{Re}	$0.5[(1 + 0.1519\sqrt{N_x})^{1/2} - 1]^2$
Unified Davis number	N_x	$\dfrac{8\,mg}{\rho_a}\left(\dfrac{A}{A_e}\right)^{1/4}$
Ice crystal mass	m (kg)	—
Area normal to the flow	A (m^2)	—
Effective area normal to the flow	A_e (m^2)	—
Dynamic viscosity of air	η (kg m^{-1} s^{-1})	$1.717 \times 10^{-5}T + 4.9 \times 10^{-8}T - 1.2 \times 10^{-10}T^2$
Surface free energy of ice	s (kg s^{-2})	0.109
Air density	ρ_a (kg m^{-3})	—
Specific heat of dry air at constant pressure	c_p (J kg^{-1} K^{-1})	1005
Specific gas constant for water vapor	R_w (J kg^{-1} K^{-1})	461.5

Blackadar, A. K., 1962: The vertical distribution of wind and turbulence exchange in neutral atmosphere. *J. Geophys. Res., 67,* 3095–3102.

Böhm, H. P., 1989: A general equation for the terminal fall speed of solid hydrometeors. *J. Atmos. Sci., 46,* 2419–2426.

Bougeault, P., 1981: Modeling the trade-wind cumulus boundary layer. Part II: A high-order one-dimensional model. *J. Atmos. Sci., 38,* 2429–2439.

Chen, J. P., and D. Lamb, 1994: Simulation of cloud microphysics and chemical processes using a multicomponent framework. Part I: Description of the microphysical model. *J. Atmos. Sci., 51,* 2613–2630.

——, G. M. McFarquhar, and A. J. Heymsfield, 1997: A modeling and observational study of the detailed microphysical structure of tropical cirrus anvils. *J. Geophys. Res., 102,* 6637–6653.

Deardorff, J. W., 1972: Numerical investigation of neutral and unstable planetary boundary layers. *J. Atmos. Sci., 29,* 91–115.

Fletcher, N. H., 1962: *The Physics of Rainclouds.* Cambridge University Press, 390 pp.

Fu, Q., and K. N. Liou, 1992: On the correlated k-distribution method for radiative transfer in nonhomogeneous atmospheres. *J. Atmos. Sci.,* **49,** 2139–2156.

——, and ——, 1993: Parameterization of the radiative properties of cirrus clouds. *J. Atmos. Sci.,* **50,** 2008–2025.

Gagin, A., 1972: The effects of supersaturation on the ice crystal production by natural aerosols. *J. Rech. Atmos.,* **6,** 175–185.

Gu, Y., and K. N. Liou, 1997a: Interactions of radiation, microphysics, and turbulence in a two-dimensional cirrus cloud model. *IRS '96: Current Problems in Atmospheric Radiation,* W. L. Smith and K. Stamnes, Eds., A. Deepak Publishing, 238–241.

——, and ——, 1997b: Numerical experiments on the interactions of various physical processes in cirrus clouds. Preprints, *Ninth Conf. on Atmospheric Radiation,* Long Beach, CA, Amer. Meteor. Soc., 97–101.

Gultepe, I., and D. O'C. Starr, 1995: Dynamical structure and turbulence in cirrus clouds: Aircraft observations during FIRE. *J. Atmos. Sci.,* **52,** 4159–4182.

Heymsfield, A. J., 1972: Ice crystal terminal velocity. *J. Atmos. Sci.,* **29,** 1348–1357.

——, 1975: Cirrus uncinus generating cells and the evolution of cirriform clouds. Part I: Aircraft observations of the growth of the ice phase. *J. Atmos. Sci.,* **32,** 799–808.

——, 1977: Precipitation development in stratiform ice clouds: A microphysical and dynamical study. *J. Atmos. Sci.,* **34,** 367–381.

——, and C. M. R. Platt, 1984: A parameterization of the particle size spectrum of ice clouds in terms of the ambient temperature and the ice water content. *J. Atmos. Sci.,* **41,** 846–855.

——, and R. M. Sabin, 1989: Cirrus crystal nucleation by homogeneous freezing of solution droplets. *J. Atmos. Sci.,* **46,** 2252–2264.

Huffman, P. J., 1973: Supersaturation spectra of AgI and natural ice nuclei. *J. Appl. Meteor.,* **12,** 1080–1082.

Jensen, E. J., O. B. Toon, D. L. Westphal, S. Kinne, and A. J. Heymsfield, 1994a: Microphysical modeling of cirrus: 1. Comparison with 1986 FIRE IFO measurements. *J. Geophys. Res.,* **99,** 10 421–10 442.

——, ——, ——, ——, and ——, 1994b: Microphysical modeling of cirrus: 2. Sensitivity studies. *J. Geophys. Res.,* **99,** 10 443–10 454.

Khvorostyanov, V. I., and K. Sassen, 1998a: Cirrus cloud simulation using explicit microphysics and radiation. Part I: Model description. *J. Atmos. Sci.,* **55,** 1808–1821.

——, and ——, 1998b: Cirrus cloud simulation using explicit microphysics and radiation. Part II: Microphysics, vapor and ice mass budgets, and optical and radiative properties. *J. Atmos. Sci.,* **55,** 1822–1845.

Klemp, J. B., and R. B. Wilhelmson, 1978: The simulation of three-dimensional convective storm dynamics. *J. Atmos. Sci.,* **35,** 1070–1110.

Krueger, S. K., 1988: Numerical simulation of tropical cumulus clouds and their interaction with the subcloud layer. *J. Atmos. Sci.,* **45,** 2221–2250.

——, and A. Bergeron, 1994: Modeling the trade wind cumulus boundary layer. *Atmos. Res.,* **33,** 169–192.

Laube, M., and H. Holler, 1988: Numerical data and functional relations in science and technology. *Cloud Phys.,* **4,** 1–110.

Lilly, D. K., 1965: On the computational stability of numerical solutions of time-dependent non-linear geophysical fluid dynamics problems. *Mon. Wea. Rev.,* **93,** 11–26.

Lin, R.-F., 1997: A numerical study of the evolution of nocturnal cirrus by a two-dimensional model with explicit microphysics. Ph.D. dissertation, The Pennsylvania State University, 198 pp. [Available from The Department of Meteorology, The Pennsylvania State University, University Park, PA 16802.]

Liou, K.-N., 1986: Influence of cirrus clouds on weather and climate processes: A global perspective. *Mon. Wea. Rev.,* **114,** 1167–1198.

——, 1992: *Radiation and Cloud Processes in the Atmosphere.* Oxford University Press, 487 pp.

——, Q. Fu, and T. P. Ackerman, 1988: A simple formulation of the delta-four-stream approximation for radiative transfer parameterizations. *J. Atmos. Sci.,* **45,** 1940–1947.

Liu, S., and S. K. Krueger, 1998: Numerical simulations of altocumulus using a cloud resolving model and a mixed layer model. *Atmos. Res.,* **47–48,** 461–474.

Mellor, G. L., and T. Yamada, 1974: A hierarchy of turbulence closure models for planetary boundary layers. *J. Atmos. Sci.,* **31,** 1791–1806.

Meyers, M. P., P. J. DeMott, and W. R. Cotton, 1992: New primary ice nucleation parameterizations in an explicit cloud model. *J. Appl. Meteor.,* **31,** 708–721.

Moeng, C.-H., 1986: Large-eddy simulation of a stratus-topped boundary layer. Part I: Structure and budgets. *J. Atmos. Sci.,* **43,** 2886–2900.

——, and Coauthors, 1996: Simulations of a stratocumulus-topped planetary boundary layer: Intercomparison among different numerical codes. *Bull. Amer. Meteor. Soc.,* **77,** 261–278.

Ou, S. C., and Coauthors, 1995: Remote sounding of cirrus cloud optical depths and ice crystal sizes from AVHRR data: Verification using FIRE II IFO measurements. *J. Atmos. Sci.,* **52,** 4143–4158.

Paluch, I. R., and C. A. Knight, 1984: Mixing and evolution of cloud droplet size spectra in a vigorous continental cumulus. *J. Atmos. Sci.,* **41,** 1801–1815.

Quante, M., P. Scheidgen, M. Laube, and E. Raschke, 1990: The structure of turbulence in cirrus clouds. Preprints, *Seventh Conf. on Atmospheric Radiation,* San Francisco, CA, Amer. Meteor. Soc., 211–218.

Ramaswamy, V., and A. Detwiler, 1986: Interdependence of radiation and microphysics in cirrus clouds. *J. Atmos. Sci.,* **43,** 2289–2301.

Starr, D. O'C., and S. K. Cox, 1985: Cirrus clouds. Part I: A cirrus cloud model. *J. Atmos. Sci.,* **42,** 2663–2681.

Takano, Y., and K. N. Liou, 1989: Solar radiative transfer in cirrus clouds. Part I: Single-scattering and optical properties of hexagonal ice crystals. *J. Atmos. Sci.,* **46,** 3–19.

Telford, J. W., and P. B. Wagner, 1981: Observations of condensation growth determined by entity type mixing. *Pure Appl. Geophys.,* **119,** 934–965.

Zhang, Y., M. Laube, and E. Raschke, 1989: Numerical studies of the time behavior of cirrostratus in still air. *Beitr. Phys. Atmos.,* **62,** 307–320.